NANO MICRO small

Supporting Information

for *Small,* DOI: 10.1002/smll.202301750

Unlocking Deep and Fast Potassium-Ion Storage through Phosphorus Heterostructure

Xiaoju Zhao, Shitao Geng, Tong Zhou, Yan Wang, Shanshan Tang, Zongtao Qu, Shuo Wang, Xiao Zhang, Qiuchen Xu, Bin Yuan, Zhaofeng Ouyang, Huisheng Peng, Shaochun Tang, and Hao Sun**

Unlocking deep and fast potassium-ion storage through phosphorus heterostructure

Xiaoju Zhao[†], Shitao Geng[†], Tong Zhou, Yan Wang, Shanshan Tang, Zongtao Qu, Shuo Wang, Xiao Zhang, Qiuchen Xu, Bin Yuan, Zhaofeng Ouyang, Huisheng Peng, Shaochun Tang* and Hao Sun*

Electrochemical measurements

GITT profiles were measured intermittently with pulse current of 100 mA g^{-1} at discharge interval of 20 min and rest interval of 1 h. The diffusion coefficients were deduced from Fick's second low as follows[1]:

$$D_k^+ = \frac{4}{\pi\tau}\left(\frac{m_B\, V_M}{M_B S}\right)^2 \left(\frac{\Delta E_s}{\Delta E_t}\right)^2$$

where D_K^+ is the K-ion diffusion coefficient, τ is the galvanostatic discharge time (s), m_B, M_B and V_M are the mass, molar mass and molar volume of the active material, respectively. V_M/M_B can be simplified as the density of active material. S is the surface area of the electrode, ΔE_s represents the voltage change at the steady state and ΔE_t represents the voltage change at galvanostatic discharge state.

The relationship between the current response and scan rate of CV curves was deduced based on following equation:

$$i = a\, v^b$$

where i and v represent current (mA) and scan rate (mV s^{-1}) respectively. a and b represent variable parameters. In this regard, b value reveals the contribution types of potassiation process. When b equals to 1.0, the redox reaction is mainly a surface capacitive process. When b equals to 0.5, the redox reaction is mainly a diffusive-controlled process. With the value of b between 0.5−1.0, both capacitive and diffusive behaviors exist, and their contribution can be quantitatively calculated based on the equation below:

$$i = i_{capacitive} + i_{diffusive} = k_1\, v + k_2\, v^{1/2}$$

where k_1v represents surface capacitive process, and $k_2v^{1/2}$ represents diffusive-controlled process.

Computational details

All the spin theoretical simulations in our work were carried out on the Vienna ab initio Simulation Package (VASP) with Version 5.4.4.[2,3] The Generalized gradient approximation (GGA) with the Perdew-Burke-Emzerhof (PBE)[4] functional form was employed to evaluate the electron-electron exchange and correlation interactions, and the projector augmented-wave (PAW) methods[5,6] were implanted to represent the core-electron (valence electron) interactions. Plane-Wave basis function was set with a kinetic cut-off energy of 550 eV. The ground-state atomic geometries were

optimized by relaxing the force below 0.02 eV/Å and the convergence criteria for energy was set with the value of 1.0×10^{-5} eV/cell. Gaussian smearing and tetrahedron method with Blöchl corrections were employed for the stress/force relaxations and electronic structures, respectively. In order to better describe the interactions between molecules, van der Waal (vdW) interactions were included descripting by zero damping DFT-D3 method of Grimme.[7,8] To investigate K-ion adsorption and diffusion for BRPH structure, black phosphorus part was modeled using a 2 × 4 supercell with two phosphorene layers, while red phosphorus part was modeled using a zig-zag ladder structure (two chains with total 28 P atoms). To investigate K-ion adsorption and diffusion inside RP interlamination, structure model with four RP chains with total 56 P atoms was used. Vacuum layer of 25 Å was set to avoid the interaction between neighboring cell in vertical direction. The Brillion zone was sampled using a 4×6×1 Monkhorst−Pack grid with Gamma centered. The transition states during K diffusion pathways were evaluated using the Climbing-image nudged elastic band (CI-NEB) method[9,10] with convergence criteria of force were below 0.05 eV/Å.

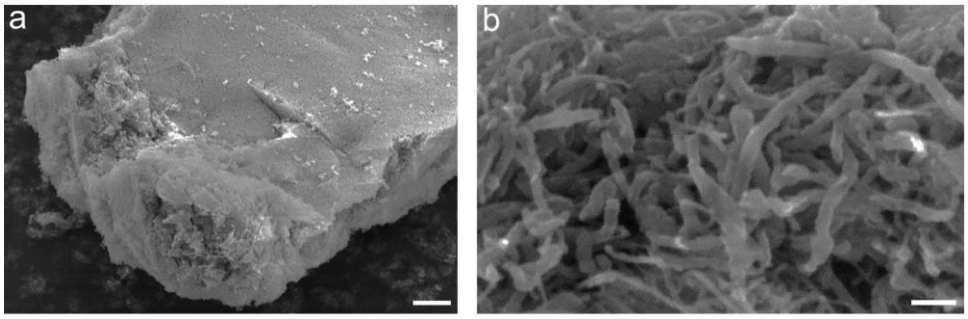

Figure S1. SEM images of the pretreated RP and RP@MWCNT, respectively. Scale bars, 1 μm (**a**) and 100 nm (**b**).

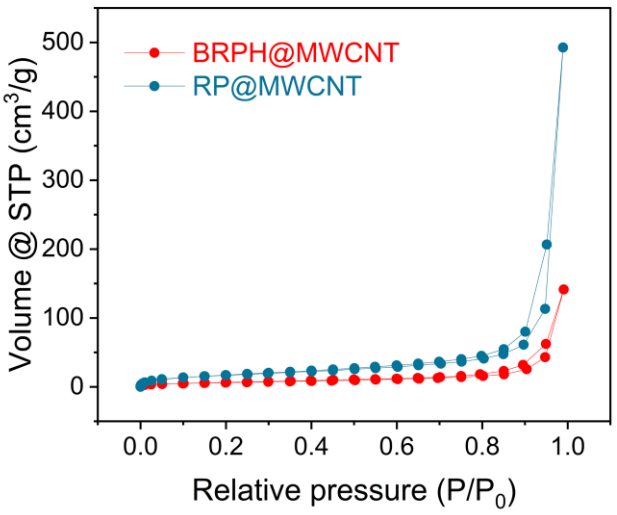

Figure S2. Nitrogen adsorption/desorption isotherms of BRPH@MWCNT and RP@MWCNT.

Based on the Brunauer-Emmett-Teller (BET) method, specific surface areas of BRPH@MWCNT and RP@MWCNT were 22.73 and 62.00 $m^2 g^{-1}$, respectively.

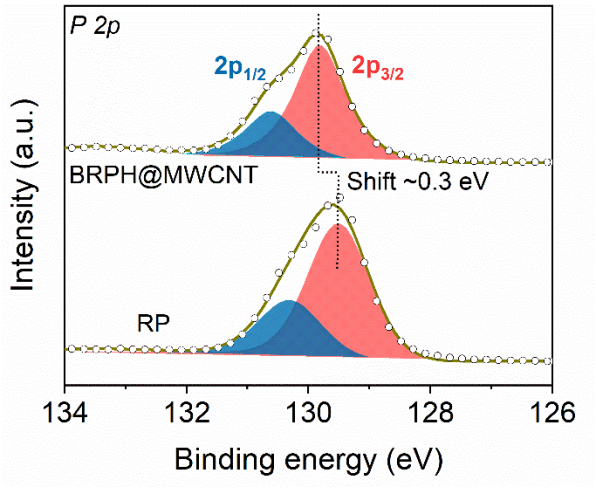

Figure S3. XPS profile of the RP and BRPH@MWCNT.

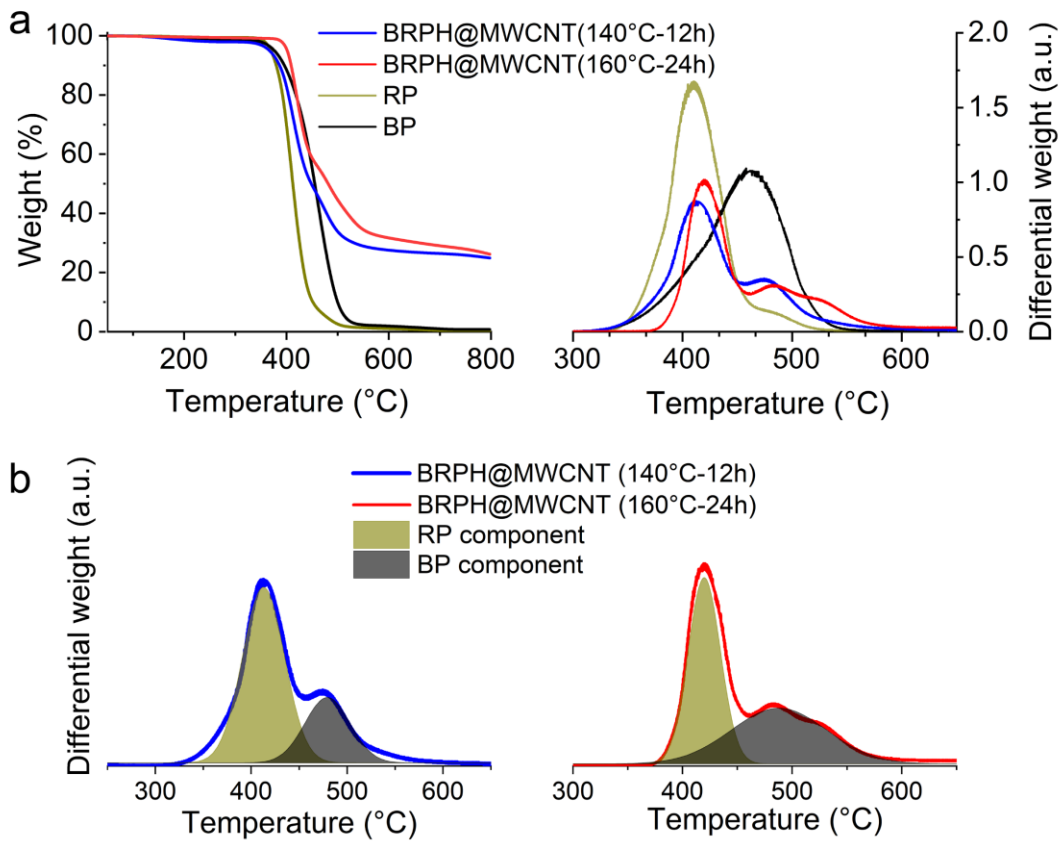

Figure S4. a, Normalized thermogravimetric (TG) analysis curves and corresponding differential thermogravimetric (-dTG) profiles of BRPH@MWCNT, RP and BP. **b,** the deconvoluted peaks of BRPH@MWCNT materials with different BP/RP ratios.

The RP counterpart in **Figure S4** was hydrothermally treated in DI water at 200 °C and BP was synthesized through the ethane diamine (EDA) solvothermal treatment of RP at 200 °C for 48 h. Two representative samples of BRPH@MWCNT were obtained based on the same EDA solvothermal procedure at **Experimental section** except for the variations of temperature and time. For instance, the BRPH@MWCNT obtained at 140 °C and 12 h, named as BRPH@MWCNT (140 °C−12 h), showed a BP/RP ratio of 0.4 based on the deconvoluted peaks in **Figure S4b**, as a comparation, the BRPH@MWCNT obtained at 160 °C and 24 h, named as BRPH@MWCNT (160 °C−24 h), showed a BP/RP ratio of 0.9 (**Figure S4b**). Thus, both temperature and time variations in the EDA-solvothermal process contributed to the BP/RP proportion of the as-synthesized heterostructure material.

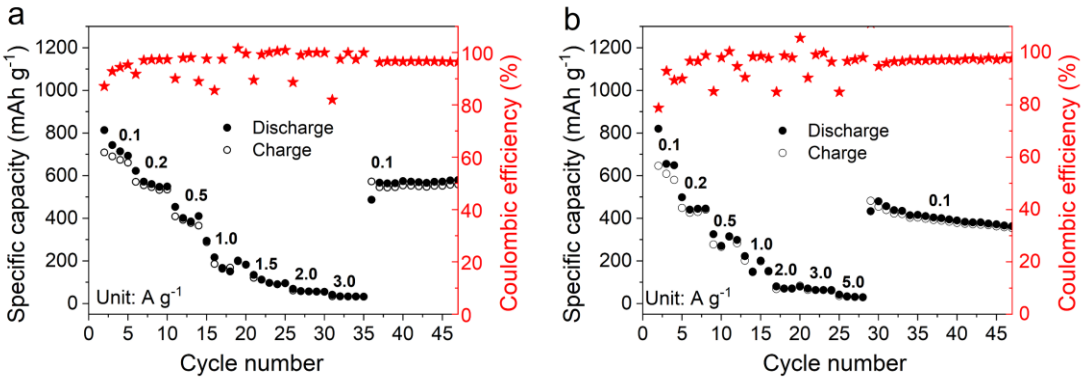

Figure S5. Rate performances of counterparts with different BP/RP ratios. **a,** BRPH@MWCNT (140 °C−12 h), BP/RP ratio: 0.4. **b,** BP@MWCNT (200 °C−48 h), BP/RP ratio: 1.0.

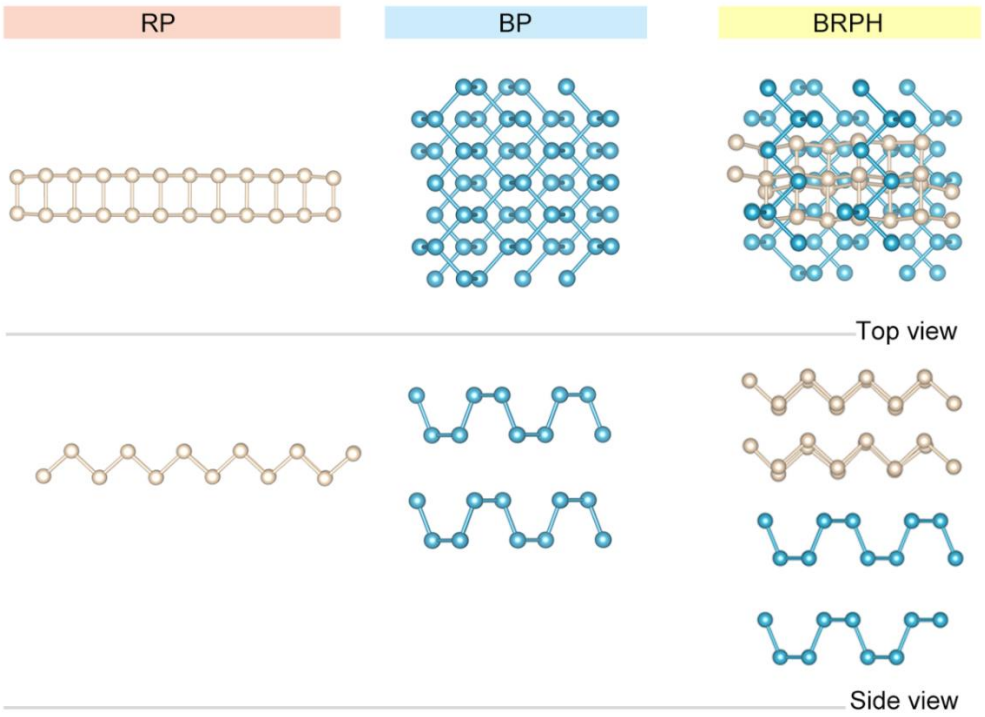

Figure S6. Structure models of RP, BP and BRPH from top and side views for DFT calculations.

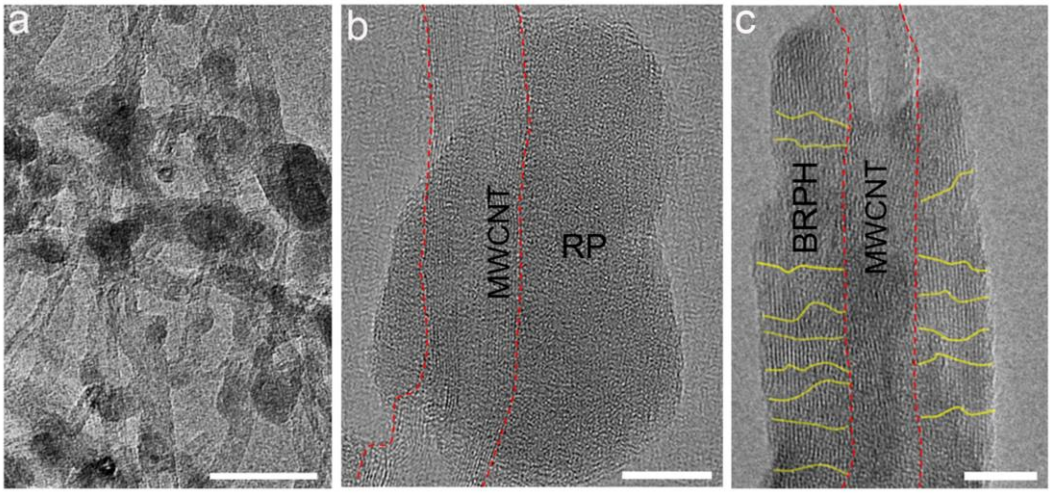

Figure S7. TEM images of the RP@MWCNT and BRPH@MWCNT. **a, b,** TEM images of RP@MWCNT. **c, d,** TEM image of BRPH@MWCNT. Scale bars are 50, 10 and 10 nm for **a**, **b** and **c**, respectively. The red and yellow lines represent MWCNT/BRPH interface and BP/RP heterointerface, respectively.

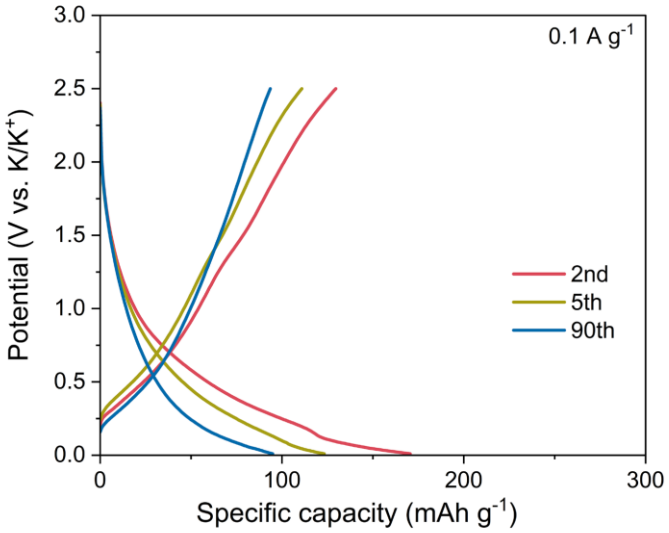

Figure S8. Galvanostatic discharge-charge curves of K metal/MWCNT half cell. The electrolyte is 4 M KFSI and 1 M KTFSI in EC/DMC (1:1 by volume). Current density, 0.1 A g^{-1}.

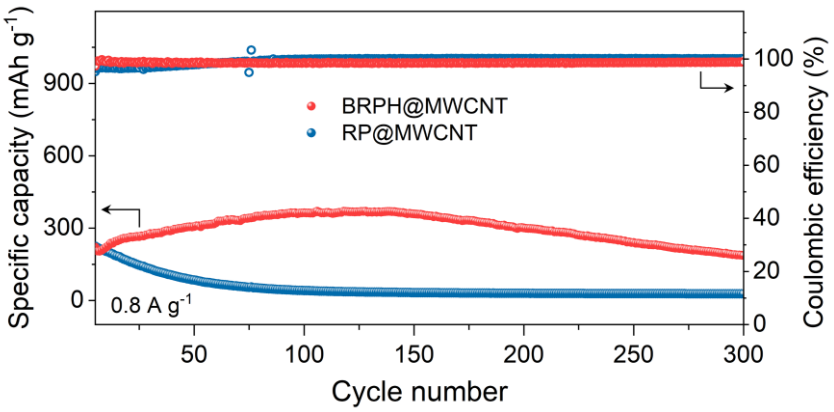

Figure S9. Cycling performance of RP@MWCNT and BRPH@MWCNT at the current density of 0.8 A g^{-1}.

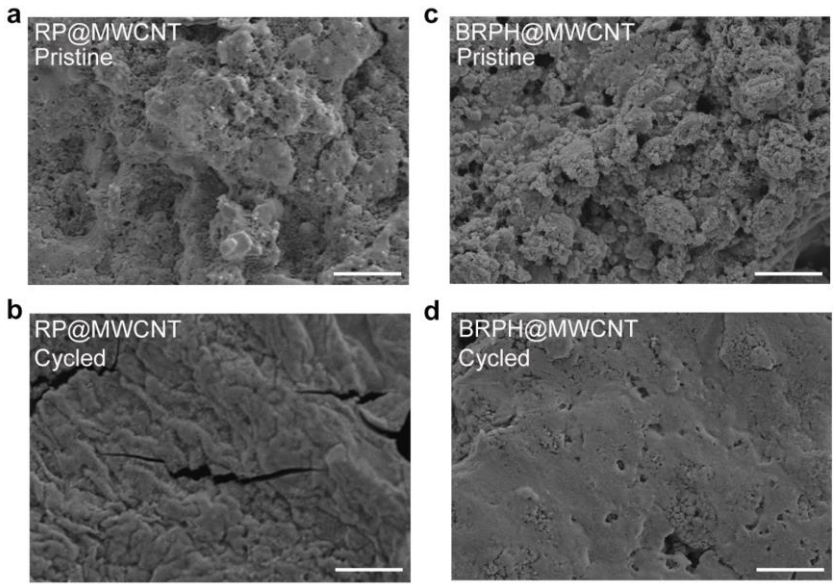

Figure S10. a, b, SEM images of RP@MWCNT anode before and after cycling for 20 cycles, respectively. **c, d,** SEM images of BRPH@MWCNT anode before and after cycling for 20 cycles, respectively. Scale bars, 2 μm.

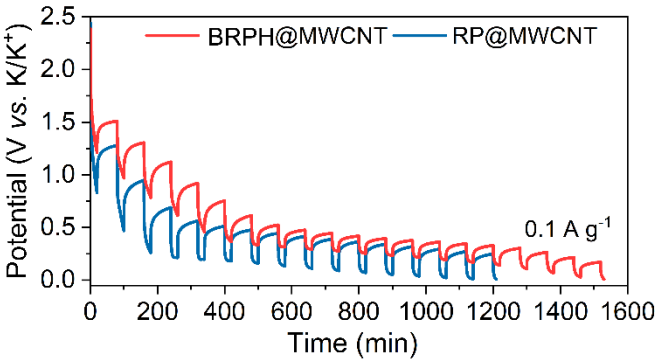

Figure S11. Galvanostatic intermittent titration (GITT) profiles of BRPH@MWCNT and RP@MWCNT anodes. Current density, 0.1 A g^{-1}.

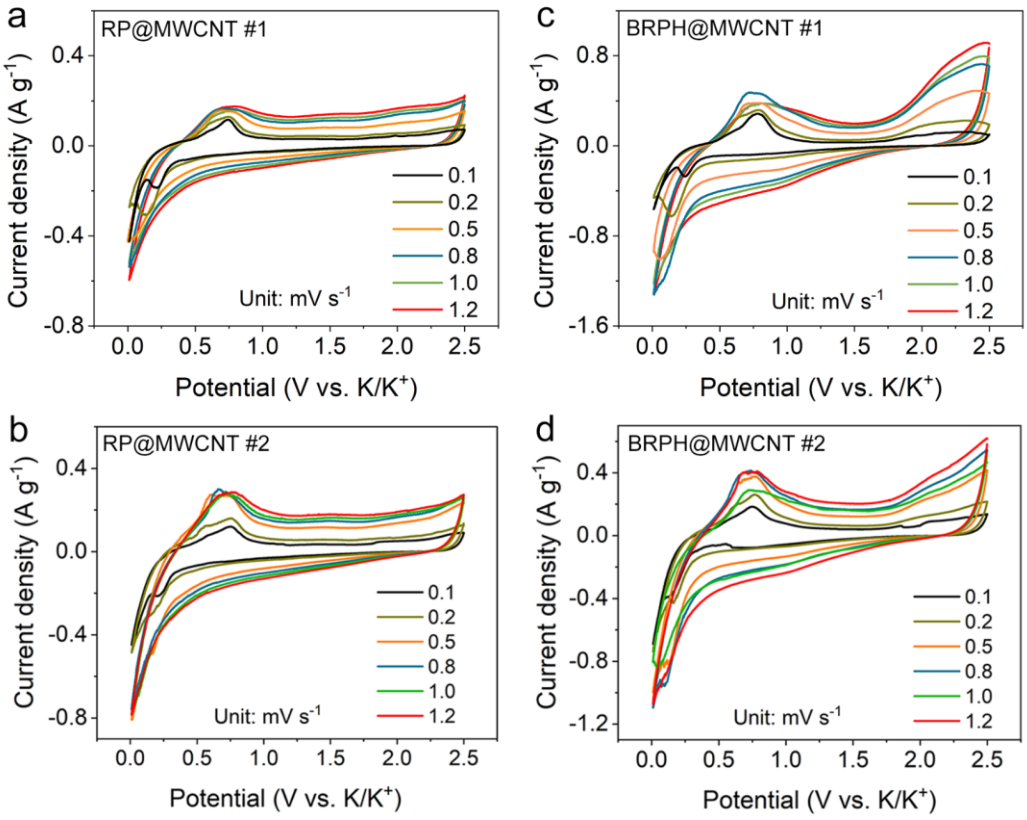

Figure S12. a, **b**, Parallel CV measurements of RP@MWCNT at various scan rates from 0.1 to 1.2 mV s^{-1}. **c, d,** Parallel CV measurements of BRPH@MWCNT at various scan rates from 0.1 to 1.2 mV s^{-1}.

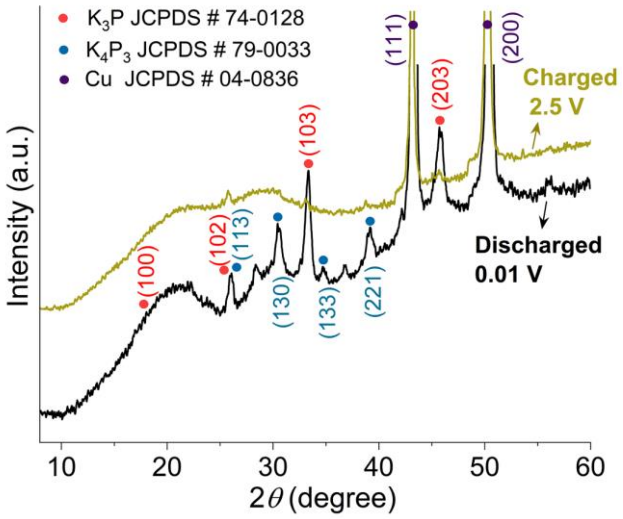

Figure S13. *Ex situ* XRD patterns of BRPH@MWCNT anodes at fully potassiated and depotassiated states.

We showed the prominent K_3P and K_4P_3 peaks in fully-discharged BRPH@MWCNT, and these peaks disappeared when further charged to 2.5 V *vs.* K/K^+.

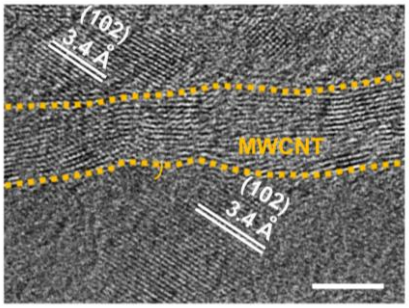

Figure S14. HRTEM analysis of BRPH@MWCNT after potassiated to 0.01 V vs. K/K^+. Scale bar, 5 nm.

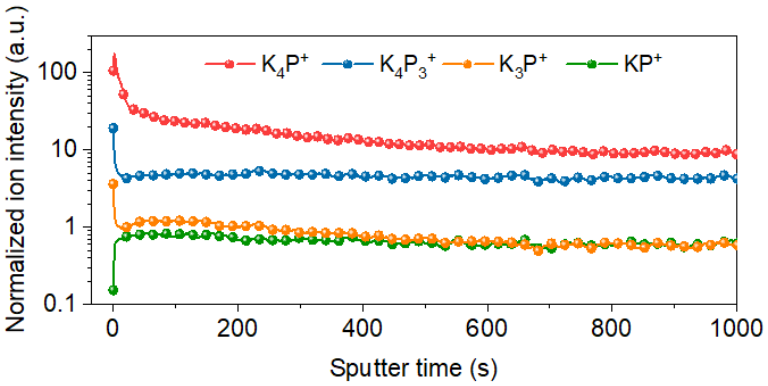

Figure S15. The normalized ion intensity of the four ion fragments (K_4P^+, $K_4P_3^+$, K_3P^+ and KP^+) as a function of sputter time of the BRPH@MWCNT anode after potassiation.

.

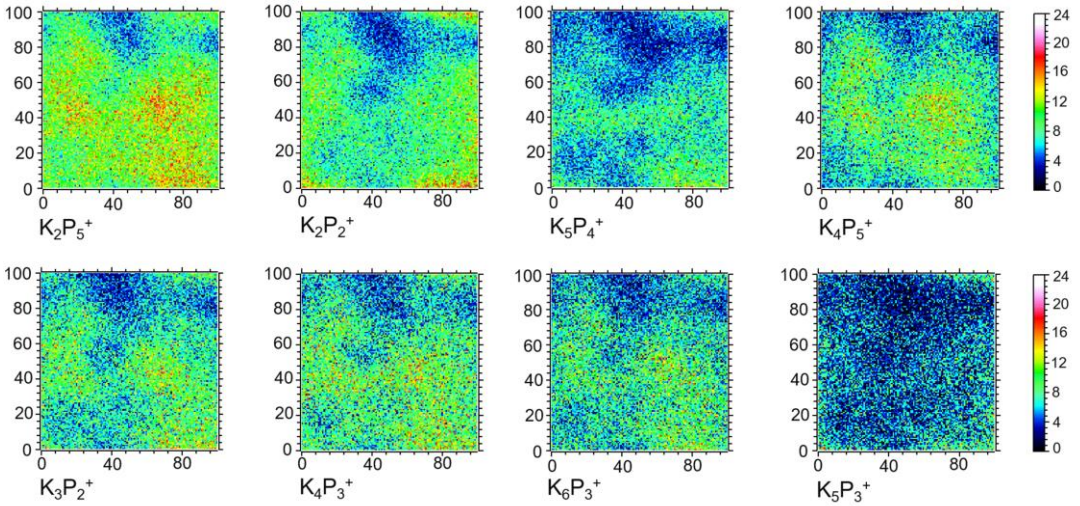

Figure S16. Intensity distributions of the main ion fragments ($K_2P_5^+$, $K_2P_2^+$, $K_5P_4^+$, $K_4P_5^+$, $K_3P_2^+$, $K_4P_3^+$, $K_6P_3^+$ and $K_5P_3^+$) of the RP@MWCNT anode after full potassiation.

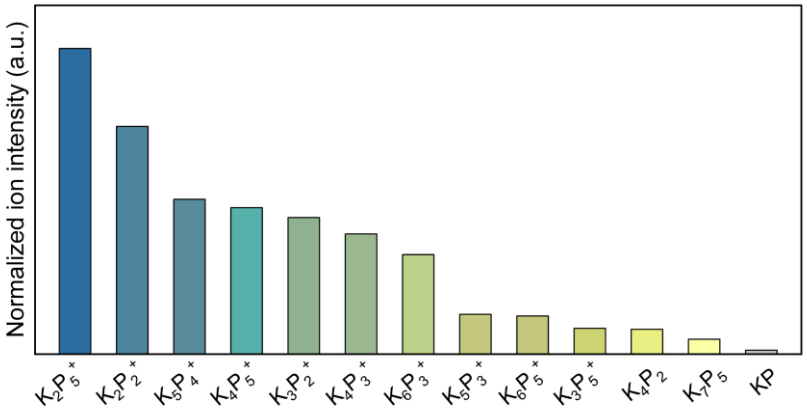

Figure S17. The normalized ion intensity of detectable ion fragments of the RP@MWCNT anode after full potassiation.

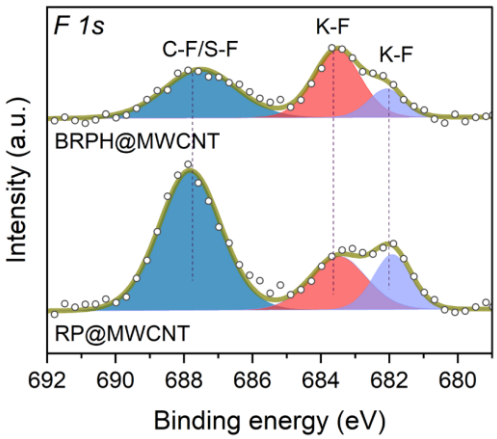

Figure S18. High-resolution XPS profile of F 1s of BRPH@MWCNT and RP@MWCNT after 20 cycles at a current density of 100 mA g^{-1}.

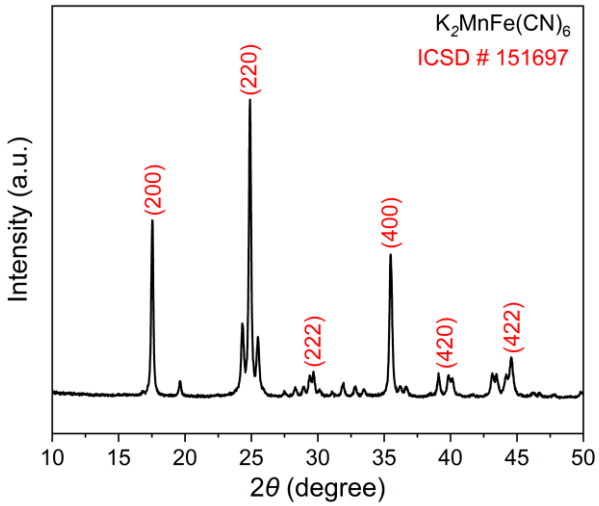

Figure S19. XRD patterns of the Prussian blue cathode.

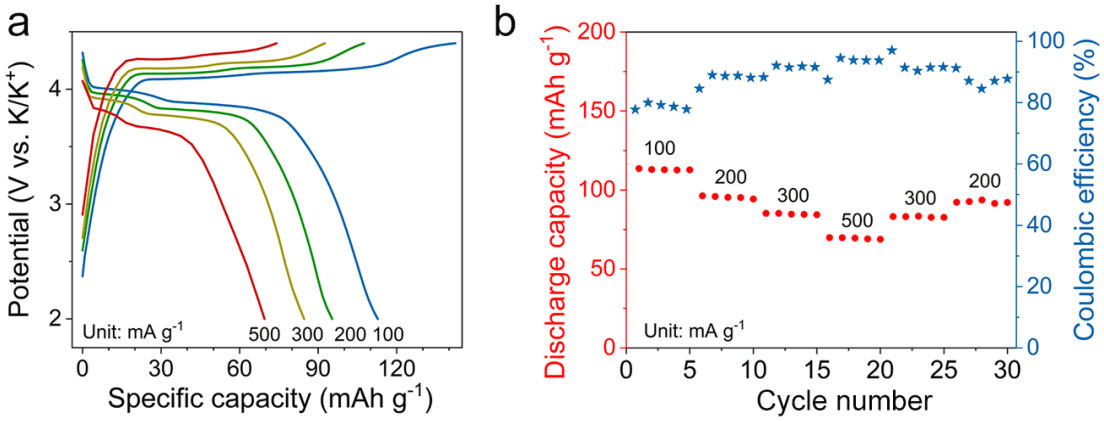

Figure S20. Rate performance of the K metal/Prussian blue half cell at various current densities from 100 to 500 mA g^{-1}.

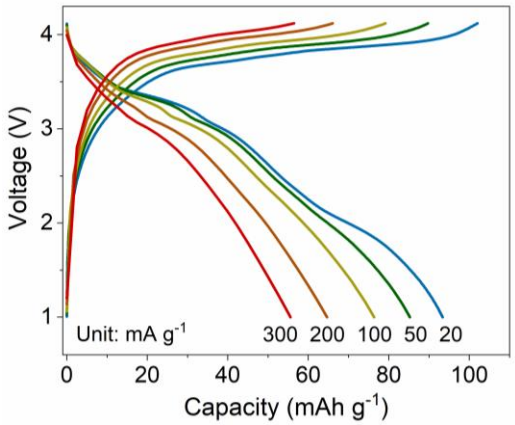

Figure S21. Rate performance of BRPH@MWCNT/Prussian blue full cell from 20 to 300 mA g^{-1} with an N/P ratio of 1.4:1.

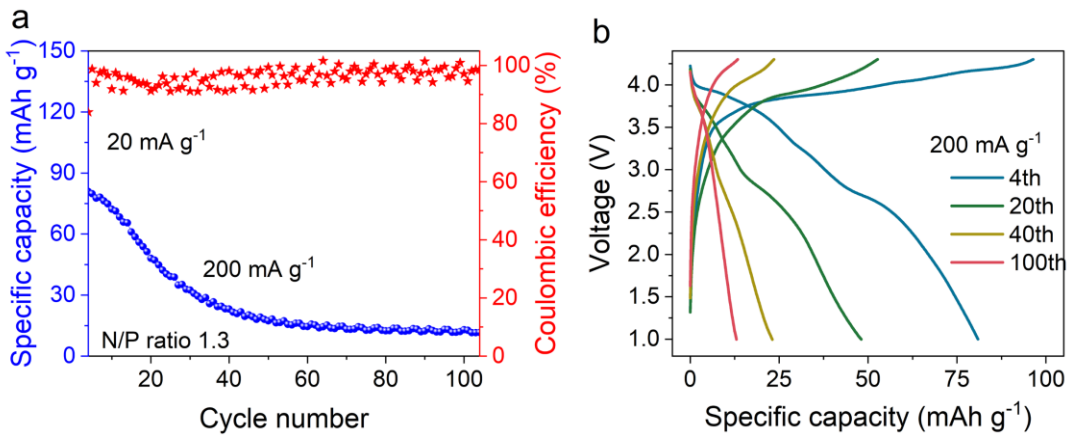

Figure S22. Cycling performance (**a**) and corresponding charge/discharge curves (**b**) of RP@MWCNT/Prussian blue full cell at 200 mA g^{-1} with the optimized N/P ratio of 1.3:1. Current density, 200 mA g^{-1}. The cell was initially charge/discharged at 20 mA g^{-1} for 3 cycles for stable SEI formation.

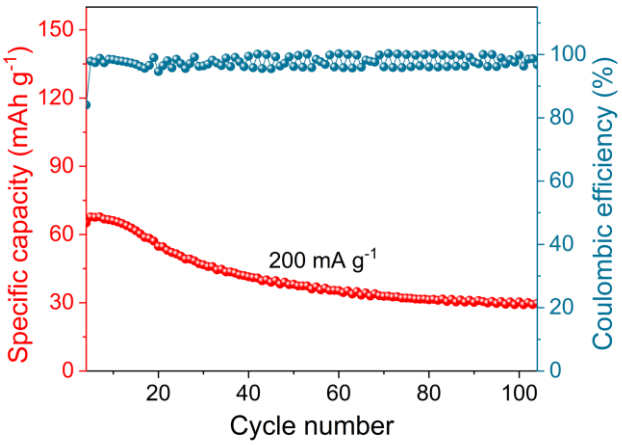

Figure S23. Cycling performance of the BRPH@MWCNT/Prussian blue full cell with a N/P ratio of 1.1. Current density, 200 mA g^{-1}. The cell was initially charge/discharged at 20 mA g^{-1} for 3 cycles for stable SEI formation.

Table S1. Comparison on the main parameters of our BRPH@MWCNT and representative elemental P-based anode materials with high P contents .

Anodes with high P contents	P percentage (wt%)	Maximal specific capacity (mAh g^{-1})	Final potassiation product	Ref.
RP@N-PHCNFs	66	700 at 0.1 A g^{-1}	K_4P_3	[11]
P/C composite	65.4	739 at 0.2 A g^{-1}	K_4P_3	[1]
P@hollow C	75	841 at 0.05 A g^{-1}	K_4P_3	[12]
P@carbon nanosheet	63.9	715 at 0.1 A g^{-1}	KP	[13]
BP/G	80	668 at 0.05 A g^{-1}	K_4P_3	[14]
P-rGO	31.5	418 at 0.1 A g^{-1}	KP	[15]
RP@S-N-CNFs	59.2	524 at 0.1 A g^{-1}	KP	[16]
BRPH@MWCNT	73.8	923 at 0.05 A g^{-1}	K_3P	This work

Table S2. Charge transfer resistance (R_{ct}) of K metal/BRPH@MWCNT and K metal/RP@MWCNT half cells during the potassiation process. Both cells were cycled at 0.1 A g^{-1} after 20 cycles and stopped at fully charged state piror to EIS measurement.

Voltage (V vs. K/K^+)	R_{ct} of BRPH@MWCNT (Ω)	R_{ct} of RP@MWCNT (Ω)
2.5	599.9	1410
1.0	598.9	1371
0.5	858.8	1204
0.4	983.7	1404
0.2	1059	2777
0.1	994.1	2830
0.01	981	7458

References

[1] W. Xiao, X. Li, B. Cao, G. Huang, C. Xie, J. Qin, H. Yang, J. Wang, X. Sun, *Nano Energy* **2021**, *83*, 105772.

[2] J. Furthmüller, G. Kresse, *Phys. Rev. B* **1996**, *54*, 11169.

[3] G. Kresse, J. Hafner, *Phys. Rev. B Condens. Matter.* **1993**, *47*, 558.

[4] J. Perdew, K. Burke, *Phys. Rev. Lett.* **1996**, *77*, 3865.

[5] G. Kresse, D. Jouert, *Phys. Rev. B* **1999**, *59*, 1758.

[6] P. E. Blochl, *Phys. Rev. B Condens. Matter.* **1994,** *50*, 17953.

[7] S. Grimme, J. Antony, S. Ehrlich, H. Krieg, *J. Chem. Phys.* **2010,** *132*, 154104.

[8] S. Grimme, S. Ehrlich, L. Goerigk, *J. Comput. Chem.* **2011,** *32*, 1456.

[9] G. Henkelman, H. Jónsson, *J. Chem. Phys.* **2000,** *113*, 9978.

[10] G. Henkelman, B. P. Uberuaga, H. Jónsson, *J. Chem. Phys.* **2000,** *113*, 9901.

[11] Y. Wu, S. Hu, R. Xu, J. Wang, Z. Peng, Q. Zhang, Y. Yu, *Nano Lett.* **2019**, *19*, 1351.

[12] X. Huang, X. Sui, W. Ji, Y. Wang, D. Qu, J. Chen, *J. Mater. Chem. A* **2020**, *8*, 7641.

[13] P. Xiong, P. Bai, S. Tu, M. Cheng, J. Zhang, J. Sun, Y. Xu, *Small* **2018**, e1802140.

[14] X. Du, B. Zhang, *ACS Nano* **2021**, *15*, 16851.

[15] X. Lu, W. Lin, Y. Huang, J. Zhang, L. Guan, X. Huang, K. Du, X. Wu, *ACS Appl. Energy Mater.* **2021**, *4*, 9682.

[16] W. Feng, H. Wang, Y. Jiang, H. Zhang, W. Luo, W. Chen, C. Shen, C. Wang, J. Wu, L. Mai, *Adv. Energy Mater.* **2022**, *12*, 2103343.